Diffusion of Brønsted Acidic Dopants in Conjugated Polymers

Journal:	*Journal of Materials Chemistry C*
Manuscript ID	TC-ART-02-2023-000415.R1
Article Type:	Paper
Date Submitted by the Author:	11-Apr-2023
Complete List of Authors:	Nguyen, Phong; University of California Santa Barbara, Schmithorst , Michael; University of California-Santa Barbara, Dept. of Chemical Engineering Mates, Tom; University of California Santa Barbara, Materials Research Laboratory Segalman, Rachel; University of California-Santa Barbara, Dept. of Chemical Engineering Chabinyc, Michael; University of California Santa Barbara, Materials

Diffusion of Brønsted Acidic Dopants in Conjugated Polymers

Phong H. Nguyen,[a] Michael B. Schmithorst,[a] Tom Mates,[c] Rachel A. Segalman [a,b,c] and Michael L. Chabinyc *[c]

Received 00th January 20xx,
Accepted 00th January 20xx

DOI: 10.1039/x0xx00000x

Many semiconductor devices (*e.g.*, light emitters and photovoltaics) utilize heterojunctions of doped and undoped layers or depend on gradients of electronic doping to control charge transport. Understanding of the formation and stability of gradients in doping requires an understanding of diffusion of dopants and the complex changes in polymer properties that arise during doping. Conjugated polymers can be electrically doped by strong acids, but the details of the reaction mechanism and subsequent stability are not understood. Here, we show a clear kinetic isotope effect in the doping of thin films of poly(3-hexylthiophene) (P3HT) by bis(trifluoromethane)sulfonimide (HTFSI) from solution indicating that this doping process is limited by proton transfer to the polymer. Complementary X-ray photoelectron spectroscopy and DSIMS depth profiling of dopant concentrations show definitive evidence of dopant enrichment at the P3HT surface. These surface-limited concentration profiles suggest that diffusivity of dopants vary inversely with dopant concentration due to doping-induced changes to the structure of the conjugated polymer.

Introduction

Electrical doping of organic semiconductors requires the incorporation of small molecules that chemically oxidize (*p*-type) or reduce (*n*-type) the organic semiconductor to form charge carriers. In many cases, dopants are added to solid thin films of semiconductors after film-casting (termed sequential doping) and consequently, controlled doping requires understanding of mass transport of the dopant into the film.[1] Doping induces complex changes to electronic, thermal, and mechanical properties alongside changes to crystalline and mesoscopic morphology.[2,3] Moreover, diffusion of dopants is a heterogeneous process owing to their semicrystalline nature which results in domains with varying electronic and ionic conductivity.[4,5] Improved control of doping requires an understanding of the reactive and diffusive driving forces for dopant transport, suitable approximations for continuum models, and consideration for the complex changes to polymer properties that arise from doping.

A common doping method involves either immersion of semiconducting polymer films in solutions of the dopant (immersion doping) or thermal evaporation/sublimation of the dopant into the polymer film (vapor doping). Both methods have been used as platforms to control and investigate the mass transport of various dopants, including 2,3,5,6-tetrafluoro-7,7,8,8-tetracyanoquinodimethane (F_4TCNQ),[6–10] molybdenum tris(1-(methoxycarbonyl)-2-(trifluoromethyl)ethane-1,2-dithiolene) (Mo(tfd-CO_2Me)$_3$),[11,12] and phosphomolybdic acid (PMA).[13] Within these studies, diffusion has been quantified in the context of: (1) diffusion of the dopant as it is introduced into the film and (2) diffusion of the dopant in the solid state following the doping process. Temperature, equilibrium between the neutral and ionized dopant, the size and shape of the dopant, the degree of solvent swelling, and doping reaction mechanism are all likely to affect the degree by which the dopant diffuses into the film.[7,10,12–15]

The most extensive models of dopant diffusion have examined the diffusion coefficients of both the neutral and ionized form of two common dopants (F_4TCNQ and Mo(tfd-CO_2Me)$_3$), both of which oxidize the conjugated polymer by a charge transfer mechanism.[6,12,16] A study of diffusion of Mo(tfd-CO_2Me)$_3$ into poly(3-hexylthiophene) (P3HT) thin films and found that the surface concentration of Mo(tfd-CO_2Me)$_3^{\bullet-}$ saturates quickly and is essentially immobilized by coupling with the charged P3HT$^{\bullet+}$.[12] A study of the in-plane diffusion of F_4TCNQ and a larger derivative (F_4MCTCNQ) in semiconducting polymers, found that the F_4TCNQ diffuses approximately 1-2 orders more quickly than its radical anion.[6] Both considered dopant adsorption capacity and found that ionized dopants are the majority species, transported predominantly through the amorphous domains.

Here, we focus on the transport of a Brønsted acidic dopant, bis(trifluoromethane)sulfonimide (HTFSI), introduced into P3HT from the solution phase. To understand the individual contributions of doping reaction and diffusion to the overall process, we first investigated the proposed Brønsted acid doping mechanism and find that proton transfer limits the overall rate of the doping reaction. By measuring the depth-dependent dopant concentrations we find that deuterium (from a labeled acid dopant) is retained in significant quantities and that doping is diffusion-limited in films >100 nm in thickness. Complementary surface-sensitive grazing incidence X-ray scattering confirms that charge carrier-induced structural changes are most concentrated at the surface, likely due to doping induced rigidity that impedes further diffusion of dopants.

---

[a] Department of Chemical Engineering, University of California, Santa Barbara, CA 93106.
[b] Department of Chemistry and Biochemistry, University of California, Santa Barbara, CA 93106.
[c] Materials Department, University of California, Santa Barbara, CA 93106.

Electronic Supplementary Information (ESI) available: [details of any supplementary information available should be included here]. See DOI: 10.1039/x0xx00000x

Results and Discussion

Thickness Dependence of Electrical Conductivity

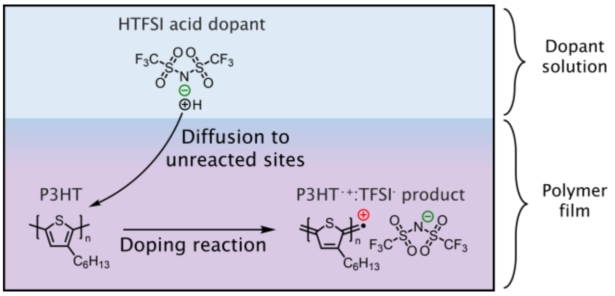

Fig. 1 Schematic of immersion doping process. First, dopants must diffuse into the polymer that is a mixture of reacted and unreacted units. Upon reaction, the polymer segment and neutral dopant are converted to the charge carrier-counterion product.

The thickness dependence of the electrical conductivity of P3HT films doped by immersion in a solution of HTFSI suggests that diffusion can limit doping. Immersion doping is a diffusive-reactive process which requires diffusion of dopants past regions of reacted polymer **(Fig. 1**). Upon diffusion to unreacted segments, the polymer segment and neutral dopant undergo a reaction to produce the charge carrier-counterion product. When 10 nm- and 265 nm-thick films of P3HT are immersed in a solution of the strong acid HTFSI, their conductivity varies inversely with film thickness. Undoped 265 nm thick films of P3HT exhibit electrical conductivities around 10^{-4} S/cm (10 nm films were 2 orders more conductive due to background doping, see **Fig. 2**). For any given set of immersion times, the thinner films exhibit conductivities approximately an order greater than those of the thicker films. The limited conductivity of the thicker film is consistent with an estimate that only the surface layer is doped. A possible interpretation is that limited diffusion of dopants can result in conductivities which vary inversely with film thickness.

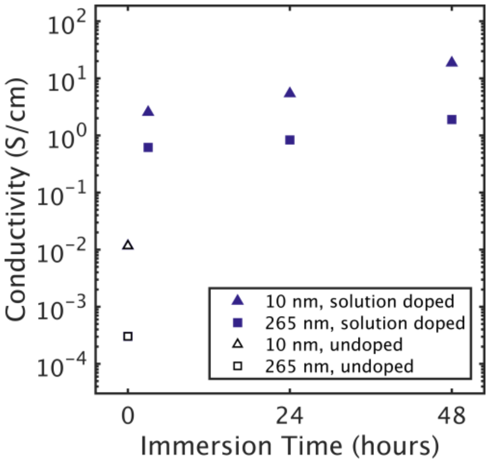

Fig. 2 Conductivity of 10 nm and 265 nm thick P3HT films immersed in acidic solutions [148 mM HTFSI (CH_3OH)] for varying times in the ambient. The fact that a much thicker film exhibits limited conductivity suggests a surface-limited doping mechanism.

Model of the Doping Process

The proposed mechanism of doping by strong Brønsted acids differs significantly from that of charge transfer dopants.[17–21] While charge transfer dopants can directly oxidize *p*-type conjugated polymers due to their high electron affinity, molecular doping via Brønsted acids have been suggested to follow a three-step mechanism, with the initial proton transfer and interchain oxidation mechanism expected to be endergonic and the final dehydrogenation step driving the reaction forward (see **Fig. 3**).[18,19,21–23] We are not aware of studies that have confirmed the proposed reaction step of loss of H_2 and a number of studies comment that the final product is unknown without proposing alternatives.[24–27] Here we investigate the overall doping reaction to first determine the rate limiting step before considering diffusion limitations.

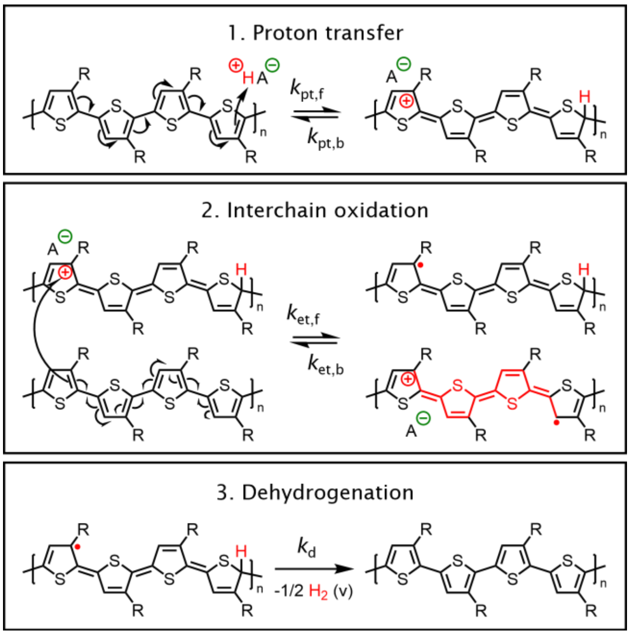

Fig. 3 Proposed mechanism of Brønsted acid doping. In the first step, the acid protonates a polymer segment, generating a charged intermediate. In the second step, the protonated intermediate oxidizes a nearby neutral segment, generating a polaron and a second hydrogenated radical intermediate. In proposed the third step, two radical intermediates react and H_2 gas is evolved.

In the first step, the polythiophene backbone (*B*) is protonated by the acid (H^+), generating a positive charge delocalized along the polymer backbone (HB^+), compensated by the counterion (A^-) (Reaction (1)).

$$\mathbf{H^+ + \boldsymbol{A}^- + \boldsymbol{B} \leftrightharpoons H\boldsymbol{B}^+ : \boldsymbol{A}^-} \qquad (1)$$

In the second step, the HB^+ intermediate oxidizes a nearby neutral chain (*B*), resulting in a hydrogenated radical intermediate ($HB^\bullet$) and polaron ($B^{\bullet+}$). Because of charge neutrality the counterion is associated with the polaron (Reaction (2)).

$$\mathbf{H\boldsymbol{B}^+ : \boldsymbol{A}^- + \boldsymbol{B} \leftrightharpoons H\boldsymbol{B}^\bullet + \boldsymbol{B}^{\bullet +} : \boldsymbol{A}^-} \qquad (2)$$

The proposed third dehydrogenation step, where two $HB^\bullet$ intermediates react and H_2 is evolved to regenerate the neutral polythiophene (*B*), is an exergonic step that drives the overall reaction forward (Reaction (3)).

$$\boldsymbol{HB^{\bullet} \rightarrow B + 1/2\,\mathrm{H_2}\ (\mathrm{v})} \tag{3}$$

To model the role of reaction rate on the immersion doping process, we consider the doping reaction by a Brønsted acid as follows. We model Reactions (1) and (2) with the assumption that the forward electron transfer is rapid and irreversible with the overall process limited by the forward rate of protonation (abbreviated as k_{pt}). With this, the observed rate of reaction is limited by the forward rate of proton transfer ($k_{\mathrm{obs}} \approx k_{\mathrm{pt}}$) Equation (4).

$$\frac{d c_{B^{\bullet+}:A^-}}{dt} = k_{\mathrm{obs}} c_{\mathrm{H}^+} \tag{4}$$

Neutral and ionized dopant transport throughout the polymer film is modeled using the diffusion-reaction equation (Equation 5).[16]

$$\frac{\partial c_i}{\partial t} = D_i \nabla^2 c_i + R_i \tag{5}$$

In Equation (5), the change in concentration with time and space of species *i* ($\partial c_i/\partial t$) is related Fickian diffusion ($D_i\nabla^2 c_i$) and reaction rate (R_i). For Reaction (4), R_i is defined for the acid dopant (H^+), polymer repeat segment (*B*), and product ($B^{\bullet+}$:A^-)) with Equation (6).

$$R_{\mathrm{H}^+} = R_B = -R_{B^{\bullet+}:A^-} = -k_{\mathrm{obs}} c_{\mathrm{H}^+} \tag{6}$$

In Equation (6), k_{obs} is the pseudo first-order rate constant of the overall reaction and $c_{\mathrm{H}+}$ is the concentration of the acid in solution.

The immersion doping experiments were controlled for dopant concentrations, film thicknesses, and immersion times to test the model. Because of the strong acidity of HTFSI (pKa < 0),[28] it is leveled by the basicity of methanol, the solvent. For all deuterated acid solutions used here, 166 mM of HTFSI was dissolved in deuterated methanol (148 molecules of CD_3OD per HTFSI) which resulted in a predominantly deuterated acid, *i.e.* $CD_3OD_2^+$. Both the acid and counter ion were tracked by DSIMS using ^{19}F and D (deuterium) as atomic labels to access the concentration profile of the dopant through the film depth.[29,30] For the diffusion-reaction model, the concentration of the acid at the film surface was approximated as constant owing to the large excess of solution relative to the total amount of polymer. The initial concentration of P3HT segments (reactant in this scenario) was varied as a fitting parameter and held fixed through each iteration. Specifically, the solid-state concentration of P3HT repeat units is calculated from its density and divided by a stoichiometric parameter to represent the average number of repeat units consumed per dopant in a reaction. Lastly, we note that the presence of oxygen did not significantly affect the doping process overall, with no resolvable differences in the depth profiles of the composition (**Fig. S4** exposed to air and **Fig. S6** entirely in N_2) using the techniques here.

Reaction Rate Limited Doping

First, we measured the primary kinetic isotope effect upon D exchange of the acidic proton to determine whether the proton transfer reaction is rate-limiting in polaron generation as assumed by the model.[31,32] To determine reaction kinetics from *in situ* UV-vis experiments, film thicknesses were minimized to 10 nm (in contrast to the 265 nm films used in depth profiling experiments). This ensures that diffusion limitations are minimized and that the changes in absorbance are determined primarily by the rate of the overall reaction. Later, relative reaction and diffusion rates were analyzed for homogeneous diffusive-reactive transport of dopants in thin films, showing that reaction kinetics can be reasonably determined from 10 nm-thick films.

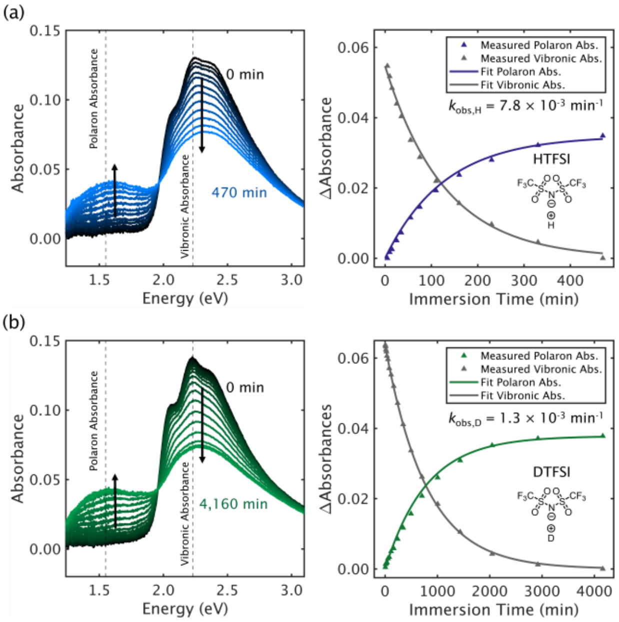

Fig. 4 (a) Time-resolved UV-vis spectra of 10 nm-thick P3HT film doped by immersion in a HTFSI solution under a nitrogen atmosphere (left). The polaron absorbance and neutral 0-1 vibronic absorbances are tracked at 1.55 and 2.23 eV, respectively, indicated by vertical dashed lines. The change in absorbance (right) reflects conversion the neutral P3HT to charged $\mathrm{P3HT}^{\bullet+}$ with immersion-doping time and is fit to a pseudo-first order rate law. (b) Time-resolved UV-vis spectra of an identically prepared 10 nm-thick P3HT film in DTFSI solution (left) and corresponding change in polaron absorbance over time.

Time-resolved UV-vis shows clear differences in the rate of polaron generation between films immersed in solutions of protonated and deuterated acid, with the DTFSI solution-doped film requiring 6 times longer than the HTFSI solution-doped film. To extract rate coefficients and assess the kinetic isotope effect, two models are employed: (1) a numerical solution to the Equation (5), to assess the full model implementation in the limiting case of no diffusion limitations, and (2) a simplified model assuming reaction-controlled kinetics and a pseudo-first order rate law.[22,33–35] The Damköhler number (Da), defined in Equation (7), describes the relative contributions of diffusion and reaction rates from Equation (5).

$$\mathbf{Da} = \frac{\textbf{reaction rate}}{\textbf{diffusion rate}} = \frac{k_{\mathrm{obs}} l^2}{D_{\mathrm{H}^+}} \tag{7}$$

In Equation (7), k_{obs} is the pseudo first-order rate of the overall reaction (able to be converted to the second-order rate constant by normalizing by the solution concentration of the acidic dopant, $c_{\mathrm{H}+,0}$),

l is the film thickness, and D_{H+} is the acid dopant diffusion coefficient. As a ratio of reaction and diffusion rates, Da $\gg$ 1 indicates a fast reaction and diffusion-limited process and Da $\ll$ 1 indicates the opposite. By minimizing the thickness of the film, the relative rate of reaction to diffusion can be minimized to allow reaction kinetics to control the time-dependent absorbance. We verify this for 10 nm P3HT films by fitting a solution to the differential mole balance that describes the time-dependent optical absorbance [Equations (8) and (9)].

$$A_B(t) = \varepsilon_B l c_B[\exp(-k_{\mathrm{obs}}t)] \qquad (8)$$

$$A_{B^{\bullet+}}(t) = \varepsilon_{B^{\bullet+}} l c_B[1 - \exp(-k_{\mathrm{obs}}t)] \qquad (9)$$

In Equation (8), $A_B(t)$ is the time-dependent change in the neutral vibronic absorbance of P3HT, ε_B is the extinction coefficient of P3HT, l is the film thickness, c_B is the P3HT polymer segment concentration (assuming 10 repeat units per segment), k_{obs} is the pseudo first-order rate of the overall reaction, and t is the reaction time. Similarly, in Equation (9), $A_{B\bullet+}(t)$ is the time-dependent change in polaron absorbance and $\varepsilon_{B\bullet+}$ is the extinction coefficient of the polaron product.

For the full diffusion-reaction system, the concentration profiles are numerically solved assuming $D_{H+} \gg k_{pt}l^2$ and converted to absorbance in the same way. Both fits to the diffusion-reaction equation (Equation (5)) and the analytical solutions to the differential mole balance (Equations (8) and (9)) result in the same reaction rate and when plotted, give overlapping curves that reinforce that doping of 10 nm films is suitable for determining reaction rate kinetics (see **Fig. S1** for comparison of fits). To fit changes in the polaron absorbance, 10 P3HT repeat units are assumed to form one reactive segment, commensurate with estimates from ENDOR measurements in similar systems.[23,36] Later, this stoichiometric parameter is varied when fitting the experimentally measured dopant concentration profiles further justifying that 10 repeat units per reactive segment is reasonable.

Upon fitting the reaction rate from protonated and deuterated acid doped films, a primary hydrogen kinetic isotope effect, $\boldsymbol{k_{pt,H}/k_{pt,D}}$ of 6, was observed. While undoped, the P3HT films exhibits well-defined vibronic absorbances between 2 eV and 2.5 eV owing to the highly aggregated and semicrystalline morphology of P3HT in the solid state. Tracking the polaronic absorbance (centered at 1.55 eV) and neutral 0-1 vibronic transition (centered at 2.23 eV) enables generation of polarons and consumption of the neutral P3HT to be monitored. On the right side of **Fig. 4**, the observed changes in polaron and vibronic absorbances are fit to Equation (5) assuming $D_{H+} \gg k_{pt}l^2$ (D_{H+} = 500 nm^2 min^{-1}). The fits closely track the change in polaronic and vibronic absorbances for both protonated and deuterated acid doped films, differing significantly only in the reaction rates (7.8 × 10^{-3} min^{-1} and 1.3 × 10^{-3} min^{-1}, respectively). From this, we conclude that the electron transfer step is fast compared to the proton transfer step and that the initial proton transfer step limits the rate of the overall reaction in the absence of limits of mass diffusion. Lastly, we note that change in absorbance features follow from the second step, thus the third dehydrogenation step is silent in the UV-vis spectra.

Stability of Protonated Polymers

To study the fate of the proton from the acidic dopant after formation of the charge carrier, we measured the retention of D using dynamic secondary ion mass spectrometry (DSIMS) (**Fig. 5**). In the case of complete retention of the acidic deuterium, D is expected to be retained in stoichiometric quantities with the TFSI$^-$ counterion. While the TFSI$^-$ concentration can be tracked by complementary XPS and DSIMS of fluorine, H/D are not accessible in XPS. Moreover, expected concentrations of D added by the labeled acid are low considering the expected doping levels and potential loss of D by the proposed dehydrogenation step. Assuming that completely doped P3HT$^{\bullet+}$ film contains 1 TFSI$^-$ per 10 repeat units, the TFSI$^-$ density should be ~10^{20} molecules cm^{-3}. The corresponding expected concentration of H and D (at natural abundance) are ~10^{23} and ~10^{19} cm^{-3}, respectively. Thus, D added by the doping process can be observed by DSIMS. Thicker P3HT films (265 nm) are used for depth profiling because of the resolution of DSIMS (~10 nm).

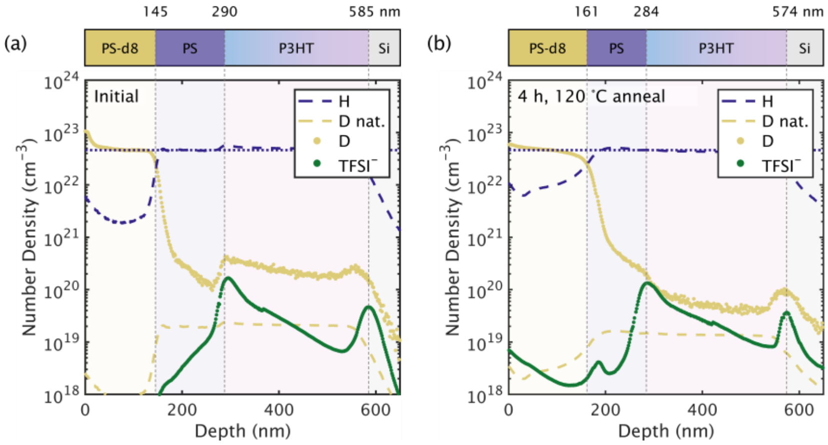

Fig. 5 Concentration depth profiles of P3HT films immersion doped in DTFSI solution for 2 days, initial (a) and annealed (b) for 4 h at 120 °C. H and D concentrations are scaled to expected densities (shown as the dotted blue line) for polystyrene-d8 and polystyrene, respectively. The concentration of D expected at natural abundance (150 ppm relative to H) is shown as a reference dashed yellow line. TFSI$^-$ concentrations are scaled to quantified XPS depth profiles of the same samples.

Concentration depth profiles (**Fig. 5**) show that the P3HT films are doped predominantly at the surface based on the TFSI$^-$ concentration (additional profiles in **Fig. S3**). For samples kept at ambient temperature, the TFSI$^-$ signal peaks upon reaching the P3HT layer and then rapidly decays indicating both immediate surface enrichment and only very limited diffusion occurring after the initial doping treatments (see **Fig. S4**). We further examined the change after thermal annealing at 120 °C for 4 hours. The similarities between the initial and annealed TFSI$^-$ profiles suggests that TFSI$^-$ diffusion is slow across a wide temperature range (ambient to 120 °C). Significant enrichment of TFSI$^-$ at the P3HT-substrate interface is an artifact of residual fluorine related to silicon wafer production.[37–39]

Our measurements of the depth profile suggest modest D enrichment of the P3HT film from reaction with DTFSI. Samples doped by DTFSI exhibit D-enrichment as compared to HTFSI-doped samples (**Fig. S3**). After drying (in vacuum of 10^{-8} torr at ambient temperature for 24 h), the total amount of D by integration [$(1.8 \pm 0.2) \times 10^{11}$] throughout the analyzed area and depth of the P3HT film exceeds the total amount of TFSI$^-$ [$(2.3 \pm 0.9) \times 10^{10}$] by an order of magnitude (**Fig. 5a**). We attribute this initial excess D to residual CD_3OD; if all the D is attributed to CD_3OD, then there are ≈2 molecules of solvent per TFSI$^-$. The amount of D decreases substantially after thermal annealing [$(5.4 \pm 1.0) \times 10^{10}$ remaining, **Fig. 5b**]. For comparison, control samples were immersed in CD_3OD solvent only and otherwise processed identically. While both control and DTFSI solution doped samples exhibited D enrichment, the control samples contained much less residual CD_3OD. This indicates that the counterion pair for the doping reaction ($CD_3OD_2^+$:TFSI$^-$) and doping of P3HT results in greater CD_3OD uptake overall. After accounting for D enrichment in the control, remaining D in equivalently processed DTFSI-doped samples suggest modest D enrichment due to the doping reaction (see **Fig. S5** and **Fig. S6**).

The final proposed step of the doping reaction is the evolution of hydrogen, but there is little direct evidence for this step in literature. Our attempts to determine the overall reaction product via NMR were inconclusive (see **Fig. S7**). The increased amount of D in the doped samples relative to our undoped control samples could either be caused by residual CD_3OD, or by reaction products where the deuteron remains in the film. The D concentration profile is relatively higher than TFSI$^-$ through the film depth. This suggests it is possible that the proposed $HB^\bullet$ intermediate (**Fig. 3**) leads to mobile $H^\bullet$ radicals that react through the thickness of the film. Given that any residual CD_3OD cannot be separated from alternative reaction products, we cannot make a conclusive determination of the final products. We also note that any reaction products with the polymer could also be accompanied by side reactions due to residual trace metal species in the polymer from synthesis. For example, it has recently been shown that Pd/Ni nanoparticles impurities from synthesis in conjugated polymers can act as hydrogen evolution catalysts in other situations.[40,41] While hydrogen evolution cannot be completely ruled out, our results suggest that other reaction products may contribute and the overall reaction could be more complex than shown in **Fig. 3**. We note that other semiconducting polymers with different backbone and sidechain designs can be doped by acids suggesting that the reaction products may vary depending on the specific material.[18,23,42–44]

Diffusion-Reaction Limited Doping

As shown in **Fig. 6**, a much slower polaron generation rate is observed for thicker films. The absorbance of the neutral polymer for 265 nm films nearly saturates the detector, thus only the polaron absorbance is tracked. Extracting the polaron absorbance at 1.55 eV shows that the reaction continues past 3,800 minutes, as compared to the 10 nm-film which saturated around 1,000 minutes. The *in situ* UV-vis spectra shows a square-like polaron absorbance, indicative of localized polarons in low concentration.[23] Using the reaction rate fit to the thinner film, we find the diffusion of the TFSI$^-$ to be significantly slower than the neutral dopant owing to its coupling with $P3HT^{\bullet+}$. As a result, assuming diffusion of only the neutral dopant results in a best-fit diffusion coefficient of 1.0 $nm^2\ min^{-1}$ ($1.7 \times 10^{-16}\ cm^2\ s^{-1}$) that approximately matches the observed rate of polaron generation. Other studies of diffusion in the solid state report the diffusion coefficient of neutral F_4TCNQ (25 °C),[6] neutral I_2 (ambient temperature),[33] and PCBM (50 °C)[45] around $10^{-11}\ cm^2\ s^{-1}$ with other studies reporting similar values.[6,33,34,45,46] A study of diffusion of the dopant, Mo(tfd-$CO_2Me)_3$, considered a similar diffusion-reaction equation (Equation (5)) and reported a diffusion coefficient between $10^{-15} - 10^{-16}\ cm^2\ s^{-1}$ and a reaction rate constant of $1.5 \times 10^{-2}\ min^{-1}$ (as compared to $7.8 \times 10^{-3}\ min^{-1}$ here).[12] We note that the dopant here is effectively the large methanoic acid-counterion pair ($CH_3OH_2^+$:TFSI$^-$) that results from the leveling effect and likely contributes to the slow diffusion observed.

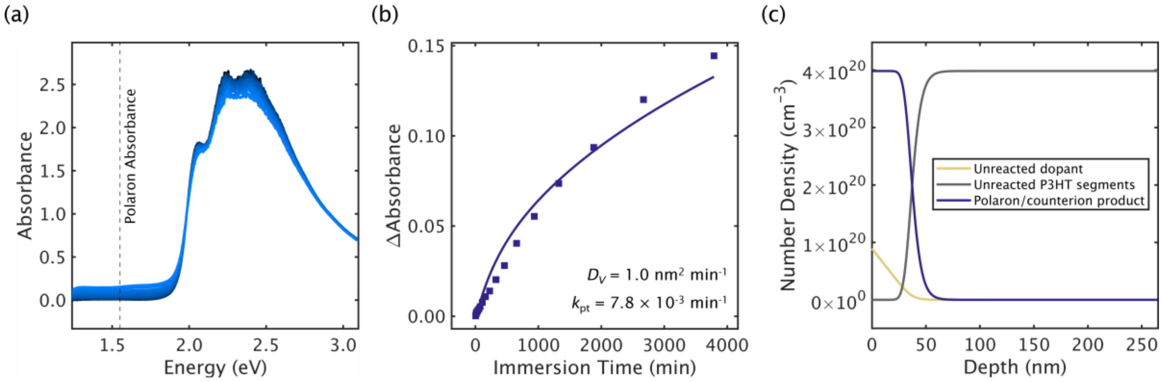

Fig. 6 (a) *In situ* UV-vis of 265 nm-thick P3HT immersion-doped in HTFSI solution. (b) Change in polaron absorbance over time fit to the diffusion-reaction model (Equation (5)), holding the same reaction rate as for the 10 nm film. (c) Predicted concentration profile from the diffusion-reaction model after 3,800 minutes (the latest data point shown in (b)).

Despite diffusion coefficient values similar those reported in literature for large dopant molecules,[6,12,33,34,45,46] our model overestimates polaron absorbance at short times and underpredicts at long times suggesting that additional considerations are needed to accurately model the rate of polaron generation. Moreover, the predicted concentration profile depicts a diffusion-limited process with a dopant saturated layer of approximately 40 nm thickness above an undoped P3HT layer (**Fig. 6c**). Because optical spectroscopy measures the through plane average concentration, some possibilities (*e.g.*, concentration-dependent dopant diffusivities) are not observable and may manifest in an apparent lower diffusion coefficient. To consider limiting factors, we assess the dopant concentration through the film depth in the context of the diffusion-reaction model.

Dopant Transport Limitations from Concentration Depth Profiles

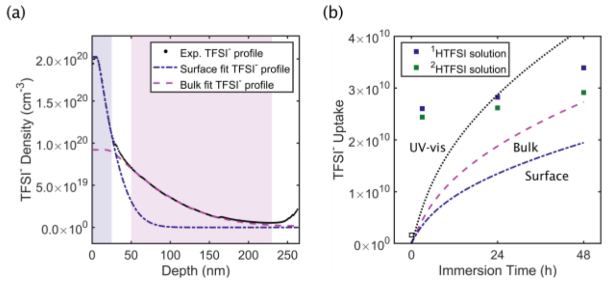

Fig. 7 (a) Depth profile of a 265 nm-thick P3HT film immersion-doped in HTFSI solution for 2 days while exposed to air. The depth profile can be fit by separating the top 20 nm (surface, blue-highlighted region) region and the remainder of the film (bulk, pink-highlighted region, 50 to 220 nm). (b) The experimentally measured total TFSI⁻ uptake in 265 nm thick P3HT films for varying immersion times in acid solutions (blue and green squares for HTFSI and DTFSI solutions, respectively) are shown alongside theoretical dopant uptake results obtained from fitting time-resolved UV-vis spectra (dotted line), the surface layer (dash-dot line), and the bulk region (dashed line). The data point at 0 minutes is a reference for the background fluorine observed in an undoped P3HT film. Details on integration and model scaling are provided in the Supplementary Information.

Upon analyzing the calibrated dopant concentration profile for the most highly doped sample (2 days of immersion in HTFSI solution with air exposure, **Fig. 7a**), it is apparent that no combination of constant diffusion coefficients can produce the experimentally observed TFSI⁻ profile. Fitting the surface region (highlighted in blue) requires approximately 5 P3HT repeat units per TFSI⁻, reflecting the high concentration of dopants in this region. Compared to the results from fitting the change in polaron absorbance for a similarly processed UV-vis sample (**Fig. 6**), the acid dopant diffusion coefficient (D_{H+}, previously assumed responsible for all of the dopant uptake) is reduced from 1.0 to 0.1 nm^2 min^{-1}. This decrease in D_{H+} is accounted for with $D_{B\bullet+:A-}$ increased to 0.2 nm^2 min^{-1} (previously assumed negligible). In contrast, when the region deeper within the film is considered (highlighted in pink), the ratio of P3HT repeat units to TFSI⁻ ions is increased from 5 to 11, consistent with lower TFSI⁻ concentration in this region. D_{H+} and $D_{B\bullet+:A-}$ are also increased from 0.1 to 0.5 nm^2 min^{-1} and 0.2 to 1.8 nm^2 min^{-1}, respectively. Altogether, differences in the fits between the surface and bulk regions suggest that regions of lower dopant concentration exhibit higher dopant diffusivity.

Comparing the model-predicted curves for the varying fit diffusivities in **Fig. 7b** to the experimentally measured dopant uptake show that concentration-dependent diffusion coefficients are needed to accurately describe dopant uptake. Earlier than 3 hours, the experimentally measured dopant uptake is much faster and drops off rapidly as compared to the model prediction. The apparent high diffusivity at short immersion doping times and apparent saturation with increasing immersion time suggest that dopant diffusivity has an inverse relationship with increasing dopant concentration. Lastly, the total TFSI⁻ uptake between HTFSI and DTFSI solution-doped films at longer times appears to vary linearly in agreement with differences their reaction rate. This is suggestive of a process where solutes must diffuse through reacted layers of increasing thickness before reaching reactive sites.[47] Altogether, these results are also consistent with recent studies which found that molecular doping nominally increases the modulus of conjugated polymers, including P3HT with a variety of dopants.[2,48,49] We propose that the immersion doping process rapidly forms a doped layer at the film surface whose rigidity limits further diffusion of the dopant and thus restricts the reaction predominantly to the top 30 nm of the film.

Doping-Induced Structural Changes Limited to Sample Surfaces

Evidence of surface-limited doped layers were further corroborated by angle resolved grazing incidence wide angle X-ray scattering (GIWAXS) measurements which show distinct doping-induced structural changes as a function of film depth. To evaluate the changes in structure of the doped films, known interplanar scattering features for pristine and doped P3HT were considered. More specifically, P3HT crystallizes with adjacent π-faces stacking in-plane and alkyl side chains stacking in the out-of-plane direction relative to the substrate.[50] For pristine P3HT, this results in scattering from the (020) and (h00) planes near 3.7 Å and 16.5 Å, respectively. Upon doping with HTFSI from the vapor phase, the alkyl chain stacking distance expands by about 1 Å from 16.5 Å and adjacent π-π stacking distances are reduced by 0.1 Å from 3.79 Å (see **Fig. S7**). Similar doping-induced structural changes have been observed for other conjugated polymers molecularly doped with TFSI⁻.[42,51,52] This is consistent with other reports using a variety of different dopants where the increase in the alkyl stacking distance is attributed to dopant counterion incorporation between inter-alkyl side chains.[50,59] The reduction in π-π stacking distance upon doping follows from polaron-induced attractive forces that assist in delocalizing polarons and helps to accommodate dopant counterions.[53] Because depth profiling measurements indicate a highly doped surface layer, differences in the structure at varying depths are expected using surface-sensitive angle resolved GIWAXS.[54–56]

Differences in the π-π stacking distance, attributed to polaron formation, were observed predominantly at the surfaces of all films. In **Fig. 8**, a complete angle resolved GIWAXS data set is shown for the most highly doped sample (a 265 nm P3HT film immersion doped in HTFSI solution for 2 days with air exposure), varying the grazing incidence angle from 0.05° to 0.13° in increments of 0.0025°. At angles less than the critical angle (0.10° for P3HT), the X-ray penetration depth is only a few nanometers, rapidly increasing to a few microns past the critical angle (**Fig. 8a**).[57] As the incidence angle varies, the resultant scattering represents depth-weighted contributions of aggregates up to the X-ray penetration depth.

Across all samples, an average difference of 0.2 Å between the (100) distance is observed at the shallowest and steepest angles, respectively (see **Table S1**). The modest increase in the dominant alkyl side chain stacking distance [(h00)] suggests that light doping throughout the film is sufficient to induce a majority of the observable inter-alkyl side chain expansion. In contrast, two π-π stacking peaks centered at 1.68 Å^{-1} and 1.75 Å^{-1}, respectively, are evident at the surface of all immersion-doped samples (**Fig. S9**). We attribute the feature at 1.68 Å^{-1} [labeled (020)] to a lightly doped aggregate population and the feature at 1.75 Å^{-1} [(020)'] to more heavily doped aggregates. Changes to the (020) π-π stacking distance vary distinctly at this doping regime, with the (020)' feature predominant at the highly doped film surface and giving way to the (020) feature past the critical angle. This is reflected in **Fig. 8b** by the relative intensity of peaks fit to each feature that vary consistently with decreasing doping levels as X-ray penetration depth increases. Similar shifts were observed during *operando* doping of P3HT in an organic electrochemical transistor with TFSI$^-$ as the counterion.[52]

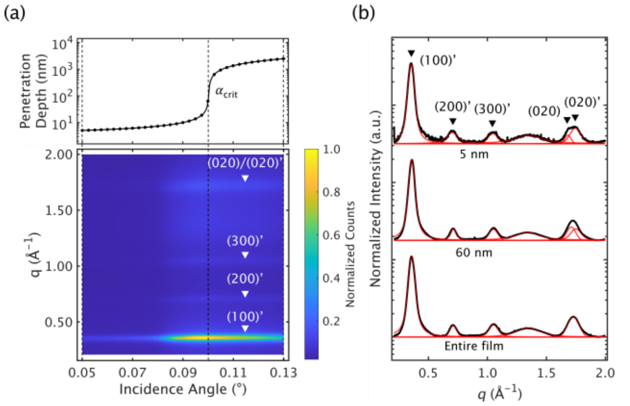

Fig. 8 Angle-dependent GIWAXS of a 265 nm-thick P3HT film immersion doped in HTFSI solution for 2 days. (a) X-ray penetration depth varies with grazing incidence angle, scattering from the top few nanometers at shallow angles to the entirety of the film thickness at greater incidence angles (top). Black dots correspond to angles at which grazing incidence measurements were taken. Surface plot of radially integrated scattering intensity versus magnitude of the scattering vector, *q*, and grazing incidence angle (bottom). (b) Radially integrated scattering intensity at the shallowest angle (0.05°, *c.a.* 5 nm), critical angle (0.10°, *c.a.* 60 nm), and deepest angle measured (0.13°, entire film), showing differences in unit cell dimensions induced by doping at the surface.

Lastly, we note that the structure of the acid doped P3HT is not significantly affected relative to other dopants. While NMR experiments were inconclusive in determining any chemical changes during doping, X-ray scattering suggests that it is unlikely to occur along the polymer backbone within ordered regions. For polythiophenes, trigonal *sp*^{2} bonding results in a planar backbone geometry that helps facilitate π-π stacking along the (020) direction. The doping-induced addition of a backbone proton bond would result in tetragonal *sp*^{3} bonding that disrupts π-π stacking structure. Instead, scattering from the acid-doped P3HT displays changes similar to those observed by other non-acidic dopants, *e.g.*, F_4TCNQ.[8] We suggest that within the doping regime here (10^{19} to 10^{20} cm^{-3}), doping in the bulk of the film takes place predominantly within disordered regions and near the disordered-ordered interfaces based on comparison with *operando* measurements of P3HT electrochemically gated with TFSI$^-$ counterions.[52]

Conclusions

Sequential doping of conjugated polymer films is a complex process due to doping-induced changes in the polymer that concomitantly affect the transport of dopants. Here we found a significant kinetic isotope effect with Brønsted acid-based doping demonstrating that proton transfer limits the rate of polaron generation in the absence of limitations of diffusion. Modest amounts of acidic deuterium are retained in doped films suggesting other possible reactions than H_2 evolution proposed in the literature. Using thicker P3HT films, we consider both reaction and diffusion processes, finding that the doping process is diffusion limited in this system. Detailed measurements of the dopant concentration profile show that the dopants are predominantly confined to the P3HT surface, suggesting an inverse relationship between doping level and dopant diffusivity. These limitations manifest in limited conductivity of thick P3HT films (as compared to uniformly doped films) as well as surface-confined doping induced structural changes. This work demonstrates that both reactive and diffusive driving forces are important for understanding the efficiency of doping processes.

Author Contributions

Nguyen, P., Chabinyc, M., Segalman, R. conceptualized the project and experiments. Nguyen, P. performed the experiments, analysis, and drafted the manuscript. Schmithorst, M. assisted with solid-state NMR experiments. Mates, T. assisted with depth profiling measurements and analysis. All authors have given approval to the final version of the manuscript.

Conflicts of interest

There are no conflicts to declare.

Acknowledgements

We acknowledge support from the U.S. Army Research Office and accomplished under cooperative agreement W911NF-19-2-0026 for the Institute for Collaborative Biotechnologies. This research made use the Stanford Synchrotron Radiation Lightsource, SLAC National Accelerator Laboratory, is supported by the U.S. Department of Energy, Office of Science, Office of Basic Energy Sciences under Contract No. DE-AC02-76SF00515. A portion of this work was performed in the UCSB Nanofabrication Facility, an open access laboratory. The research reported here made use of shared facilities of the National Science Foundation Materials Research Science and Engineering Center (MRSEC) at UC Santa Barbara (NSF DMR 1720256), which is a member of the Materials Research Facilities Network (www.mrfn.org). P.H.N gratefully acknowledges support from the National Science Foundation Graduate Research Fellowship Program under grant no. 2139319. Any opinions, findings, and conclusions or recommendations expressed in this material are those of the authors and do not necessarily reflect the views of the National Science Foundation.

Notes and references

1 I. E. Jacobs and A. J. Moulé, *Advanced Materials*, 2017, **29**, 1703063.

2 S. Zokaei, D. Kim, E. Järsvall, A. M. Fenton, A. R. Weisen, S. Hultmark, P. H. Nguyen, A. M. Matheson, A. Lund, R. Kroon, M. L. Chabinyc, E. D. Gomez, I. Zozoulenko and C. Müller, *Materials Horizons*, 2022, **9**, 433–443.

3 E. Lim, A. M. Glaudell, R. Miller and M. L. Chabinyc, *Advanced Electronic Materials*, 2019, **5**, 1800915.

4 C. Cendra, A. Giovannitti, A. Savva, V. Venkatraman, I. McCulloch, A. Salleo, S. Inal and J. Rivnay, *Advanced Functional Materials*, 2019, **29**, 1807034.

5 V. N. Prigodin, F. C. Hsu, J. H. Park, O. Waldmann and A. J. Epstein, *Phys. Rev. B*, 2008, **78**, 035203.

6 J. Li, C. Koshnick, S. O. Diallo, S. Ackling, D. M. Huang, I. E. Jacobs, T. F. Harrelson, K. Hong, G. Zhang, J. Beckett, M. Mascal and A. J. Moulé, *Macromolecules*, 2017, **50**, 5476–5489.

7 I. E. Jacobs, E. W. Aasen, J. L. Oliveira, T. N. Fonseca, J. D. Roehling, J. Li, G. Zhang, M. P. Augustine, M. Mascal and A. J. Moulé, *Journal of Materials Chemistry C*, 2016, **4**, 3454–3466.

8 E. Lim, K. A. Peterson, G. M. Su and M. L. Chabinyc, *Chem. Mater.*, 2018, **30**, 998–1010.

9 K. Kang, S. Watanabe, K. Broch, A. Sepe, A. Brown, I. Nasrallah, M. Nikolka, Z. Fei, M. Heeney, D. Matsumoto, K. Marumoto, H. Tanaka, S. Kuroda and H. Sirringhaus, *Nature Materials*, 2016, **15**, 896–902.

10 M. F. DiTusa, G. L. Grocke, T. Ma and S. N. Patel, *Molecular Systems Design & Engineering*, , DOI:10.1039/D1ME00192B.

11 A. Dai, A. Wan, C. Magee, Y. Zhang, S. Barlow, S. R. Marder and A. Kahn, *Organic Electronics*, 2015, **23**, 151–157.

12 P. Reiser, L. Müller, V. Sivanesan, R. Lovrincic, S. Barlow, S. R. Marder, A. Pucci, W. Jaegermann, E. Mankel and S. Beck, *J. Phys. Chem. C*, 2018, **122**, 14518–14527.

13 V. A. Kolesov, C. Fuentes-Hernandez, W.-F. Chou, N. Aizawa, F. A. Larrain, M. Wang, A. Perrotta, S. Choi, S. Graham, G. C. Bazan, T.-Q. Nguyen, S. R. Marder and B. Kippelen, *Nature Mater*, 2017, **16**, 474–480.

14 E. M. Thomas, K. A. Peterson, A. H. Balzer, D. Rawlings, N. Stingelin, R. A. Segalman and M. L. Chabinyc, *Advanced Electronic Materials*, 2020, **6**, 2000595.

15 M. T. Fontana, D. A. Stanfield, D. T. Scholes, K. J. Winchell, S. H. Tolbert and B. J. Schwartz, *J. Phys. Chem. C*, 2019, **123**, 22711–22724.

16 L. Yu, D. Scheunemann, A. Lund, D. Kiefer and C. Müller, *Appl. Phys. Lett.*, 2021, **119**, 181902.

17 E. Poverenov, N. Zamoshchik, A. Patra, Y. Ridelman and M. Bendikov, *J. Am. Chem. Soc.*, 2014, **136**, 5138–5149.

18 P. Simón Marqués, G. Londi, B. Yurash, T.-Q. Nguyen, S. Barlow, S. R. Marder and D. Beljonne, *Chemical Science*, 2021, **12**, 7012–7022.

19 C. C. Han and R. L. Elsenbaumer, *Synthetic Metals*, 1989, **30**, 123–131.

20 C. R. Bridges and T. Baumgartner, *Journal of Physical Organic Chemistry*, 2020, **33**, e4077.

21 E. H. Suh, J. G. Oh, J. Jung, S. H. Noh, T. S. Lee and J. Jang, *Advanced Energy Materials*, 2020, **10**, 2002521.

22 S. A. Gregory, Y. Li, T. D. Monroe, J. Li, S. K. Yee and M. D. Losego, *ACS Appl. Polym. Mater.*, 2021, **3**, 720–729.

23 M. Arvind, C. E. Tait, M. Guerrini, J. Krumland, A. M. Valencia, C. Cocchi, A. E. Mansour, N. Koch, S. Barlow, S. R. Marder, J. Behrends and D. Neher, *J. Phys. Chem. B*, 2020, **124**, 7694–7708.

24 B. Yurash, D. X. Cao, V. V. Brus, D. Leifert, M. Wang, A. Dixon, M. Seifrid, A. E. Mansour, D. Lungwitz, T. Liu, P. J. Santiago, K. R. Graham, N. Koch, G. C. Bazan and T.-Q. Nguyen, *Nat. Mater.*, 2019, **18**, 1327–1334.

25 C. Yin, M. Mukaida, S. Horike, K. Kirihara, S. Yamane, Z. Zhang and Q. Wei, *RSC Advances*, 2022, **12**, 6748–6754.

26 S. A. Chen and M. Y. Hua, *Macromolecules*, 1993, **26**, 7108–7110.

27 M.-Y. Hua, S.-W. Yang and S.-A. Chen, *Chem. Mater.*, 1997, **9**, 2750–2754.

28 E. Raamat, K. Kaupmees, G. Ovsjannikov, A. Trummal, A. Kütt, J. Saame, I. Koppel, I. Kaljurand, L. Lipping, T. Rodima, V. Pihl, I. A. Koppel and I. Leito, *Journal of Physical Organic Chemistry*, 2013, **26**, 162–170.

29 J. C. Aguirre, S. A. Hawks, A. S. Ferreira, P. Yee, S. Subramaniyan, S. A. Jenekhe, S. H. Tolbert and B. J. Schwartz, *Advanced Energy Materials*, 2015, **5**, 1402020.

30 D. T. Scholes, P. Y. Yee, J. R. Lindemuth, H. Kang, J. Onorato, R. Ghosh, C. K. Luscombe, F. C. Spano, S. H. Tolbert and B. J. Schwartz, *Advanced Functional Materials*, 2017, **27**, 1702654.

31 L. Melander and W. H. Saunders, *Reaction rates of isotopic molecules*, Wiley, 1980.

32 S. Jhulki, H.-I. Un, Y.-F. Ding, C. Risko, S. K. Mohapatra, J. Pei, S. Barlow and S. R. Marder, *Chem*, 2021, **7**, 1050–1065.

33 A. J. Maliakal, *ACS Appl. Mater. Interfaces*, 2013, **5**, 8300–8307.

34 V. Vijayakumar, E. Zaborova, L. Biniek, H. Zeng, L. Herrmann, A. Carvalho, O. Boyron, N. Leclerc and M. Brinkmann, *ACS Appl. Mater. Interfaces*, 2019, **11**, 4942–4953.

35 Y. Zhong, V. Untilova, D. Muller, S. Guchait, C. Kiefer, L. Herrmann, N. Zimmermann, M. Brosset, T. Heiser and M. Brinkmann, *Advanced Functional Materials*, **n/a**, 2202075.

36 A. Aguirre, P. Gast, S. Orlinskii, I. Akimoto, E. J. J. Groenen, H. E. Mkami, E. Goovaerts and S. V. Doorslaer, *Phys. Chem. Chem. Phys.*, 2008, **10**, 7129–7138.

37 V. R. Deline, W. Katz, C. A. Evans and P. Williams, *Appl. Phys. Lett.*, 1978, **33**, 832–835.

38 S. Surana, T. Conard, C. Fleischmann, J. G. Tait, J. P. Bastos, E. Voroshazi, R. Havelund, M. Turbiez, P. Louette, A. Felten, C. Poleunis, A. Delcorte and W. Vandervorst, *J. Phys. Chem. C*, 2016, **120**, 28074–28082.

39 V. S. Smentkowski, G. Zorn, A. Misner, G. Parthasarathy, A. Couture, E. Tallarek and B. Hagenhoff, *Journal of Vacuum Science & Technology A*, 2013, **31**, 030601.

40 J. Kosco, M. Sachs, R. Godin, M. Kirkus, L. Francas, M. Bidwell, M. Qureshi, D. Anjum, J. R. Durrant and I. McCulloch, *Advanced Energy Materials*, 2018, **8**, 1802181.

41 M. Sachs, H. Cha, J. Kosco, C. M. Aitchison, L. Francàs, S. Corby, C.-L. Chiang, A. A. Wilson, R. Godin, A. Fahey-Williams, A. I. Cooper, R. S. Sprick, I. McCulloch and J. R. Durrant, *J. Am. Chem. Soc.*, 2020, **142**, 14574–14587.

42 E. M. Thomas, E. C. Davidson, R. Katsumata, R. A. Segalman and M. L. Chabinyc, *ACS Macro Lett.*, 2018, **7**, 1492–1497.

43 S. N. Patel, A. M. Glaudell, D. Kiefer and M. L. Chabinyc, *ACS Macro Lett.*, 2016, **5**, 268–272.

44 R. Kroon, A. I. Hofmann, L. Yu, A. Lund and C. Müller, *Chem. Mater.*, 2019, **31**, 2770–2777.

45 N. D. Treat, T. E. Mates, C. J. Hawker, E. J. Kramer and M. L. Chabinyc, *Macromolecules*, 2013, **46**, 1002–1007.

46 G. A. Berriman, J. L. Holdsworth, X. Zhou, W. J. Belcher and P. C. Dastoor, *AIP Advances*, 2015, **5**, 097220.

47 E. L. Cussler and E. L. Cussler, *Diffusion: mass transfer in fluid systems*, Cambridge university press, 2009.

48 J. Moulton and P. Smith, *Polymer*, 1992, **33**, 2340–2347.

49 J. Hynynen, E. Järsvall, R. Kroon, Y. Zhang, S. Barlow, S. R. Marder, M. Kemerink, A. Lund and C. Müller, *ACS Macro Lett.*, 2019, **8**, 70–76.

50 D. Dudenko, A. Kiersnowski, J. Shu, W. Pisula, D. Sebastiani, H. W. Spiess and M. R. Hansen, *Angewandte Chemie International Edition*, 2012, **51**, 11068–11072.

51 A. I. Hofmann, R. Kroon, L. Yu and C. Müller, *J. Mater. Chem. C*, 2018, **6**, 6905–6910.

52 E. Thomas, presented in part at the APS March Meeting, November, 2018.

53 W. Liu, L. Müller, S. Ma, S. Barlow, S. R. Marder, W. Kowalsky, A. Köhn and R. Lovrincic, *J. Phys. Chem. C*, 2018, **122**, 27983–27990.

54 R. Joseph Kline, M. D. McGehee and M. F. Toney, *Nature Mater*, 2006, **5**, 222–228.

55 Z. Jiang, D. R. Lee, S. Narayanan, J. Wang and S. K. Sinha, *Phys. Rev. B*, 2011, **84**, 075440.

56 E. Gann, M. Caironi, Y.-Y. Noh, Y.-H. Kim and C. R. McNeill, *Macromolecules*, 2018, **51**, 2979–2987.

57 B. J. Factor, T. P. Russell and M. F. Toney, *Macromolecules*, 1993, **26**, 2847–2859.